nature astronomy

Article

https://doi.org/10.1038/s41550-023-02107-5

Salts and organics on Ganymede's surface observed by the JIRAM spectrometer onboard Juno

Received: 12 December 2022

Accepted: 18 September 2023

Published online: 30 October 2023

Check for updates

Federico Tosi[1] ✉, Alessandro Mura[1], Alessandra Cofano[1], Francesca Zambon[1], Christopher R. Glein[2], Mauro Ciarniello[1], Jonathan I. Lunine[3], Giuseppe Piccioni[1], Christina Plainaki[4], Roberto Sordini[1], Alberto Adriani[1], Scott J. Bolton[2], Candice J. Hansen[5], Tom A. Nordheim[6], Alessandro Moirano[1,7], Livio Agostini[1], Francesca Altieri[1], Shawn M. Brooks[6], Andrea Cicchetti[1], Bianca Maria Dinelli[8], Davide Grassi[1], Alessandra Migliorini[1], Maria Luisa Moriconi[1], Raffaella Noschese[1], Pietro Scarica[1], Giuseppe Sindoni[4], Stefania Stefani[1] & Diego Turrini[9]

The surface of Ganymede exhibits diversity in composition, interpreted as indicative of geological age differences between dark and bright terrains. Observations from Galileo and Earth-based telescopes have revealed the presence of both water ice and non-ice material, indicative of either endogenic or exogenic processes, or some combination. However, these observations attained a spatial resolution that was too coarse to reveal the surface composition at a local scale. Here we present the high-spatial-resolution infrared spectra of Ganymede observed with the Jovian InfraRed Auroral Mapper onboard the National Aeronautics and Space Administration's Juno spacecraft during a close flyby that occurred on 7 June 2021. We found that at a pixel resolution <1 km, the surface of Ganymede exhibits signatures diagnostic of hydrated sodium chloride, ammonium chloride and sodium/ammonium carbonate, as well as organic compounds, possibly including aliphatic aldehydes. Carbon dioxide shows up mostly at trailing longitudes. The composition and spatial distribution of these salts and organics suggest that their origin is endogenic, resulting from the extrusion of subsurface brines, whose chemistry reflects the water–rock interaction inside Ganymede.

The surface composition of icy satellites, beyond the ubiquitous presence of water ice, is an outstanding question with important implications. The composition can provide clues to the origin and evolution of the body, and thus may set the stage for habitability. Subsurface liquid water oceans, when present, may interact with the icy surfaces above, directly bearing on ocean habitability and detection of possible tracers of extraterrestrial life. The simultaneous presence of endogenous and exogenous compounds creates challenges in probing the composition

[1]Istituto Nazionale di Astrofisica–Istituto di Astrofisica e Planetologia Spaziali, Rome, Italy. [2]Southwest Research Institute, San Antonio, TX, USA. [3]Cornell University, Ithaca, NY, USA. [4]Agenzia Spaziale Italiana, Rome, Italy. [5]Planetary Science Institute, Tucson, AZ, USA. [6]Jet Propulsion Laboratory, California Institute of Technology, Pasadena, CA, USA. [7]Università degli Studi di Roma 'La Sapienza', Rome, Italy. [8]Consiglio Nazionale delle Ricerche–Istituto di Scienze dell'Atmosfera e del Clima, Bologna, Italy. [9]Istituto Nazionale di Astrofisica–Osservatorio Astrofisico di Torino, Pino Torinese, TO, Italy.
✉e-mail: federico.tosi@inaf.it

Table 1 | JIRAM spectral slits and geometric circumstances

Slit no.	Filename	UTC time	Altitude (km)	JIRAM nominal pixel resolution (km)	Phase angle (°)	Solar incidence angle (°)	Emission angle (°)	Local solar time (h)
1	JIR_SPE_RDR_2021158T165730_V01.DAT	7 June 2021 16:57:26	1,316.5	0.313	83.4–79.9	73.9–75.6	10.3–5.5	7.2–7.1
2	JIR_SPE_RDR_2021158T165800_V01.DAT	7 June 2021 16:57:56	1,551.2	0.369	83.3–79.8	61.9–64.1	22.7–17.2	8.1–8.0
3	JIR_SPE_RDR_2021158T165830_V01.DAT	7 June 2021 16:58:27	1,843.2	0.438	83.2–79.6	48.9–52.0	36.5–30.1	9.1–8.9
4	JIR_SPE_RDR_2021158T165900_V01.DAT	7 June 2021 16:58:57	2,181.9	0.519	82.6–79.1	34.4–39.1	50.3–42.0	10.2–9.9
5	JIR_SPE_RDR_2021158T165930_V01.DAT	7 June 2021 16:59:27	2,558.2	0.608	82.3–78.9	14.3–23.1	75.7–59.8	11.9–11.1

For each of the five spectral slits used in this work, we list the Planetary Data System (PDS) filename, acquisition time at mid-exposure and some geometric information, such as altitude over the surface, nominal pixel resolution, phase angle (calculated relative to the surface), solar incidence angle, emission angle and local solar time. The five slits were acquired in a 2 min period and in the altitude range of 1,317–2,558 km above the surface, yielding unprecedented nominal pixel resolution values between 0.31 and 0.61 km (mean value of 0.45 km). The effective spatial resolution is affected by smearing in the along-track direction. However, this does not coincide with the slit's major axis, so that adjacent pixels observe quite different areas.

of the internal oceans thought to be present in 'ocean worlds', especially in the Jovian system, that is, Ganymede and Europa. Because Ganymede has a substantially thicker crust than Europa (for example, refs. 1,2), exchanges between its deeper interior and surface may not be responsible for its surface composition, and thus may reflect exchange between the shallow crust and surface, or exogenous deposition.

Infrared observations of Ganymede returned by the Galileo Near Infrared Mapping Spectrometer (NIMS)[3] achieved broadly regional coverage at spatial-resolution values of 100 to 150 km per pixel (ref. 4). Those data suggested the presence of non-water ice materials, specifically hydrated minerals revealed by asymmetries or distortions observed in the main absorption bands of water ice and differences in reflectance compared to that expected from pure ice[5]. Such spectral characteristics were associated primarily with dark terrains and were initially interpreted as salt minerals, such as magnesium and sodium sulfate hydrates, as evidence of endogenic processes. Similar processes have been proposed to occur on Europa[6]. Recently, Earth-based spectroscopic observations achieving a spatial resolution of tens of kilometres per pixel have suggested the presence of chlorinated salts as an alternative to the sulfate salts explanation for the distortions observed in the water ice bands on both Europa and Ganymede[7,8]. The reddish-brown colour associated with the young geological features of Europa has been interpreted as a result of irradiated sodium chloride[9]. Here, we use high-spatial-resolution infrared data from the Juno spacecraft's closest flyby of Ganymede to derive new constraints on the composition of Ganymede's surface.

Results

The JIRAM dataset

The Jovian Infrared Auroral Mapper (JIRAM)[10] onboard the National Aeronautics and Space Administration's (NASA) Juno spacecraft[11] combines a double L- and M-band infrared imager and a slit spectrometer covering the wavelength range from 2 to 5 μm with an average spectral sampling of 9 nm. The instantaneous field of view (FoV) of the instrument is 238 μrad, giving a spatial resolution (pixel size) of ~2.38 km at 10,000 km.

On 7 June 2021, the spacecraft flew within ~1,046 km of Ganymede's surface, providing the opportunity for JIRAM to acquire five spectral slits and related infrared images on the satellite's day side shortly after the closest approach[12] (Table 1). The nominal spatial resolution of the five JIRAM slits was <1 km, a factor of 3–5 times higher than that of the most resolved hyperspectral image previously acquired by Galileo/NIMS[4]. Observations with JIRAM during earlier orbits provided comparative spectra of much larger regions at a resolution of tens of km[13]. Correcting for stray light (Methods), the average spectral profile of Ganymede during the close flyby differs from previous JIRAM spectral profiles (Fig. 1 and Supplementary Figs. 1–3) and from those obtained by Galileo/NIMS in the past.

Several spectral features (*f*) emerged from the average spectrum measured by JIRAM (Fig. 1b). In ascending order of wavelengths, those with a good signal-to-noise ratio (Methods) are seen at 2.08 μm (*f*1), 2.54 μm (*f*2), 2.89 μm (*f*3), 3.00 μm (*f*4), 3.48 μm (*f*5), 3.58 μm (*f*6), 3.65 μm (*f*7) and 4.25 μm (*f*8). Further inflections and very to extremely weak absorption bands are noted at about 2.22, 2.42, 2.60, 2.82, 3.05, 3.16, 3.25 and 3.38 μm.

Comparison with laboratory data

Here, we use Extended Data Table 1 along with the stacked plots in Supplementary Figs. 4–11 to investigate potential assignments for the spectral signatures observed by JIRAM based on numerous spectral endmembers measured in the laboratory in the spectral range of 2–5 μm. We discuss the spectral signatures in ascending wavelength order.

The *f*1 band centred at 2.08 μm is not compatible with pure crystalline ice, whose absorption in that spectral region is centred at 2.02 μm, that is, in the short-wavelength edge of the JIRAM sensitivity range. This indicates that ice is mixed with other compounds that have an absorption centred at this wavelength, such as NH_4Cl, $NaCl{\cdot}2H_2O$ or bloedite, which is a hydrated sodium magnesium sulfate mineral ($Na_2Mg(SO_4)_2{\cdot}4H_2O$).

JIRAM observed very weak spectral signatures at 2.22 and 2.42 μm. The band at 2.22 μm, which does not appear in water ice, can be ascribed to NH_4Cl, NaCl, $MgCl_2{\cdot}6H_2O$, $NaHCO_3$, $Na_2CO_3{\cdot}2NaHCO_3{\cdot}3H_2O$ (trona) or $(NH_4)_2CO_3$. The inflection seen at 2.42 μm is consistent with $MgCl_2{\cdot}6H_2O$ and $MgSO_4{\cdot}6H_2O$. Nitrate salts have diagnostic absorptions around 2.06, 2.21 and 2.42 μm, which may overlap with water bands and whose exact position may vary depending on the cation in the nitrate salt[14]. However, they have much stronger bands beyond 2.5 μm, which did not appear in the JIRAM spectra. Hydrated silica also exhibits absorption bands at 2.21–2.22 μm due to Al/Si–OH combination tones, with an additional, weak OH band at 2.42 μm, possibly diagnostic of hydrous phyllosilicates, such as smectites. On the other hand, $CaCl_2$ has two spectral signatures at 2.23 and 2.60 μm.

The weak *f*2 band at 2.54 μm is a typical characteristic of hydrated chloride compounds, such as $NaCl{\cdot}2H_2O$, $CaCl_2{\cdot}6H_2O$ and $MgCl_2{\cdot}2H_2O$; carbonates, such as $NaHCO_3$, Na_2CO_3 and $CaCO_3$; and the sulfate bloedite. Pure granular water ice displays a feature at 2.50 μm, especially for ultrafine to intermediate grain size. However, the position and shape of *f*2 favour these contaminants compared to the case of pure ice.

https://doi.org/10.1038/s41550-023-02107-5

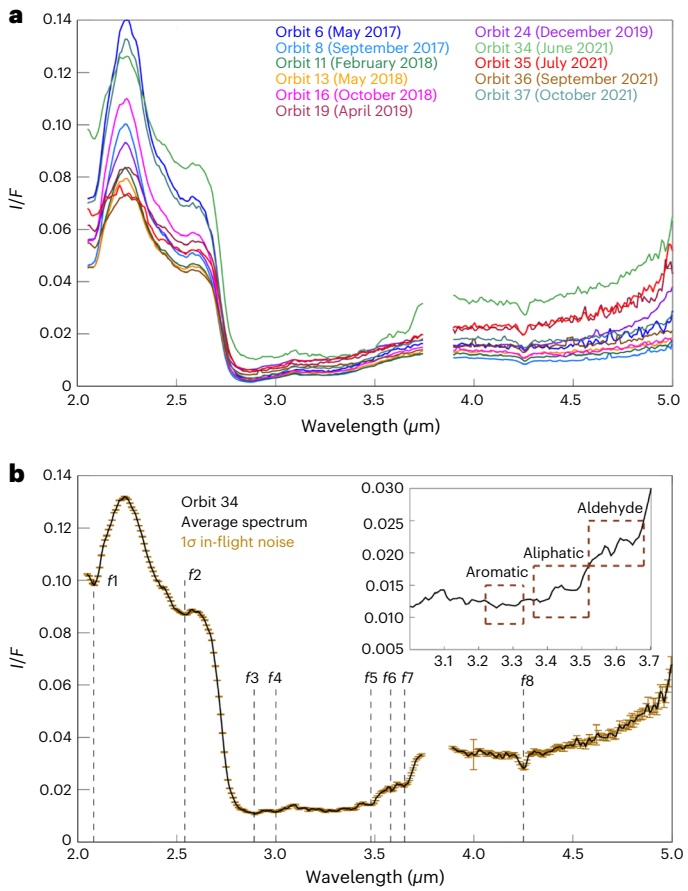

Fig. 1 | Average spectral profile of Ganymede as observed by Juno/JIRAM. **a**, Average spectral profiles of Ganymede acquired by JIRAM and displayed in units of calibrated radiance factor (*I*/*F* where *I* is the radiance measured from the target and *F* is the instantaneous solar radiance scaled by the heliocentric distance) in several flybys where spectroscopic data of good quality could be obtained. A different colour corresponds to a different average spectrum and Juno orbit. In all cases, data were filtered in such a way as to retain only those pixels with a solar illumination angle and an emission angle of less than 75° to increase the signal-to-noise ratio. The gap at 3.8 μm corresponds to a permanent artefact[10]. All spectral profiles show a prominent absorption at ~2.9 μm, which is the main signature of water, as well as a weaker absorption at 4.25 μm due to trapped/complexed carbon dioxide (CO_2). **b**, Details of the average profile obtained in orbit 34 on 7 June 2021 with error bars and vertical dashed lines highlighting the position of the main spectral signatures. Data are presented as the mean values of 1,179 pixels ± s.e.m. measured on the sky background during the same observation sequence (Methods). The upper-right inset is a close-up of the region of organics between 3.0 and 3.7 μm, where dashed brown boxes highlight regions diagnostic of aromatic, aliphatic and aldehyde compounds.

The strong absorption *f*3 seen at 2.89 μm is the fundamental O–H stretching transition active in water ice, as well as in hydrated and hydroxylated minerals. In the hydrated salt minerals considered in Extended Data Table 1, the minimum of this band generally varies between 2.86 and 3.08 μm, with 2.89 μm being akin to $NaCl{\cdot}2H_2O$ and $MgCl_2{\cdot}6H_2O$.

The 3.00 μm *f*4 band is compatible with Na_2SO_4 (weakly hydrated, as measured in the laboratory) and $(NH_4)_2SO_4$, although signatures at 3.01 and 3.16 μm could also be due to water adsorbed/bound in phyllosilicates[15]. The NH_4-bearing phases display diagnostic absorptions in the range of 3.01–3.08 μm (ref. 16). The ν_3 absorption in NH_4 is variable and is likely related to the degree of hydrogen bonding of the NH_4–H_2O complexes[17], which could explain the very weak signature seen by JIRAM at 3.05 μm. The reflectance peak around 3.10 μm is due to Fresnel reflection off the facets in the water ice grains (for example, ref. 18).

The *f*5 band at 3.48 μm is compatible with carbonate salts, such as $NaHCO_3$, Na_2CO_3, $CaCO_3$ and $(NH_4)_2CO_3$, but also with several organics. Similarly, the *f*6 band at 3.58 μm could be matched by $CaCl_2$ and $CaCO_3$, as well as by organics.

Among the salts of endogenous origin, chlorides show a larger number of positive detections compared to the spectral signatures measured by JIRAM, including weak and very weak signatures, although Ca and Mg chlorides have substantially different profiles, especially beyond 3 μm, whereas $NaCl{\cdot}2H_2O$ and NH_4Cl are more plausible. Within sulfate salts, Ca, Na, and NH_4 sulfates can be safely ruled out because they have substantially different spectral shapes both between 2.0 and 2.7 μm and beyond 3.5 μm. Bloedite appears to be the sulfate salt that best mimics the shape measured by JIRAM. Carbonates represent an intermediate case between chlorides and sulfates in terms of positive spectral detections, although Ca and Na carbonates should display a strong absorption close to 4 μm, which is unseen in the JIRAM spectra, making $NaHCO_3$ or $(NH_4)_2CO_3$ more plausible options.

The overall 3.0–3.7 μm range is diagnostic of organics. The existence of organic compounds on Callisto and Ganymede had first been suggested based on a spectral signature at 3.4 μm detected in NIMS data, associated with the $-CH_3/CH_2$ stretch in aliphatic organics or in tholins[5,19]. The earlier more distant observations by Juno/JIRAM supported the finding of organics, but a concrete identification was not possible[13]. In the JIRAM dataset discussed here, an extremely weak signature appears at 3.25 μm, within the 1σ instrumental noise. Aromatic hydrocarbons display a =C–H signature in the 3.22–3.33 μm range[20], which in principle might explain this feature. As for aliphatic alkane compounds, the $-CH_3$ (methyl) asymmetric stretch has a spectral counterpart in the range of 3.36–3.39 μm, while the symmetric $-CH_3$ stretch has a counterpart in the 3.47–3.49 μm range[20]. Similarly, the asymmetric stretch $-CH_2$ (methylene) has a spectral counterpart at 3.40–3.45 μm, while the symmetric stretch occurs at 3.49–3.52 μm (ref. 20). A very weak band at 3.38 μm in the JIRAM average spectrum, at the limit of 1σ noise, suggests that a methyl group is more likely to be present (or more abundant) than a methylene group. The weak *f*7 3.65 μm band could be due to aryl ($Ar–CH_3$) or alkyl (RCHO) groups[21,22]. The simultaneous presence of two features *f*6 at 3.58 μm and *f*7 at 3.65 μm could be indicative of aldehydic C–H vibrations, while the carbonyl group stretch C=O is beyond the wavelength range of JIRAM.

The feature *f*8 at 4.25 μm is the diagnostic signature of carbon dioxide (CO_2). Because free CO_2 ice has an absorption centred at 4.27 μm, the surface of Ganymede has trapped/complexed CO_2, that is, CO_2 is mixed with something else in the uppermost millimetre-thick surface layer to produce the observed shift[23].

The JIRAM data do not reveal, or are not decisive in revealing, any spectral signatures of exogenously produced compounds, such as hydrogen peroxide or hydrated sulfuric acid (Supplementary Fig. 11). Both compounds were detected on Europa[24,25] and at high latitudes on Ganymede[8,26,27]; however, in the spectral range of 2.0–2.5 μm where the JIRAM data and laboratory spectra overlap, hydrated sulfuric acid has no diagnostic signatures. The strongest signatures of hydrogen peroxide in the near-infrared range of 2–5 μm are due to the water solution, while the most diagnostic signature already observed on Europa, that is, the one centred at 3.505 μm[24], is not detected on Ganymede beyond the JIRAM instrumental noise. Furthermore, the JIRAM spectra do not reveal signatures at 4.07 and 4.37 μm, diagnostic of sulfur dioxide (SO_2)[28,29]. SO_2 was convincingly identified on Europa and Callisto and has been suggested to be associated with the implantation of magnetospheric S ions that originate from volcanic activity on Io[30].

Linear spectral unmixing is suboptimal with the JIRAM spectroscopic data obtained on Ganymede, and its results may be misleading (Methods and Supplementary Information). Evaluating the position of the spectral signatures and making comparisons with an ample

number of meaningful laboratory spectra are a better approach for interpreting the JIRAM data.

Mapping the JIRAM spectroscopic data

The JIRAM spectral profiles reveal variability due to the changing illumination and observation conditions and to the different terrains sampled along the sequence (Fig. 2 and Supplementary Fig. 12). The JIRAM data spanned a narrow range of latitudes (10° N to 30° N) and a wider range of longitudes (−35° E to +40° E) in the sub-Jovian hemisphere, covering a variety of geological units, such as grooved terrains, bright ejecta and dark terrains (Supplementary Fig. 13). This area was not covered by previous NIMS observations, except for slit 5, where the NIMS coverage had a very coarse spatial resolution[4]. The maximum pixel resolution, and consequently the least coverage, is obtained in the first slit, whereas the following slits show a pixel resolution that progressively decreases with increasing coverage and distance from Ganymede. The spectral slits initially covered a branch of Phrygia Sulcus north of Tros crater (slit 1), mapped as intermediate light subdued material[31], then moved from west to east covering a dark terrain unit classified as dark lineated/dark cratered material[31] (slit 2), then the bright ejecta of a small fresh crater mapped as young light grooved material[31] (slit 3), then another portion of Phrygia Sulcus northeast of Nanshe Catena, partly classified as dark cratered material and partly as old/intermediate light subdued material[31] (slit 4), and finally, a larger area consisting of an intertwining of different terrains, including dark cratered material, young and old light grooved material, and old/intermediate light subdued material[31] (slit 5).

Closeups of the JIRAM ground footprints revealed spatial variations in the strength of some absorption bands (Fig. 3, Fig. 4, Fig. 5 and Supplementary Fig. 14), allowing the investigation of correlations with geological features and correlations among individual spectral signatures (Methods). While neither strong nor systematic correlations emerge between any pair of spectral signatures, weak correlations and anticorrelations may arise between band depths (BDs) within each JIRAM slit, indicative of a variable degree of mixing between different species, such as water, salts and organics, in different terrains. The composition can vary according to the terrain type, and a larger abundance of non-ice compounds is not necessarily found only in dark terrains but also in some grooved terrains, albeit with compositional differences between different grooves, suggesting that an endogenic process, such as the extrusion of subsurface brines, may determine the observed composition. The complexed CO_2 signature at 4.25 μm is weak in slits 1–3 covering leading longitudes, while it is stronger in slits 4 and 5 covering trailing longitudes (Fig. 2, Figs. 3-5). CO_2 hardly shows any correlation with other spectral signatures, except in slit 2, which sampled a dark terrain, indicating that the distribution of CO_2 in the JIRAM coverage may not depend on the occurrence of other non-ice species considered here. Not all dark terrains appear to be equally enriched in CO_2, which is also consistent with a distribution controlled by geological processes[32].

Discussion

The composition observed by JIRAM on Ganymede at the local scale could be a mixture of $NaCl{\cdot}2H_2O$, NH_4Cl, $NaHCO_3$ or $(NH_4)_2CO_3$, and $Na_2Mg(SO_4)_2{\cdot}4H_2O$, presumably the solid residue of the deep-ocean brine that reached the surface. The new higher-resolution data also suggest the presence of the alkane methyl group $-CH_3$, possibly associated with aliphatic aldehydes. Aldehydes, which play an important role as prebiotic precursor molecules, have been found in carbonaceous chondrites[33] and potentially in Enceladus plume ice grains[34] and may result from liquid water activity[35]. Modelling indicates that Ganymede's low-latitude/equatorial surface regions are shielded from electrons with energies up to approximately 40 MeV (ref. 36). The latitudes of the sub-Jovian/trailing hemisphere are also shielded from heavy ions with energies up to at least hundreds of kiloelectron volt[37,38]. Therefore, it is expected that the surface composition examined by JIRAM will be minimally affected by radiation processing.

Other outer Solar System bodies have salts and organics that have been identified as being of endogenic origin. This is most evident on Enceladus, where sodium salts (NaCl, $NaHCO_3$ and/or Na_2CO_3) were identified in the plume material directly sampled by mass spectrometry[39]. A similar composition has also been found in the Cerealia Tholus dome at the centre of the Occator crater on Ceres, where a mixture of $Na_2CO_3{\cdot}H_2O$, $NaCl{\cdot}2H_2O$ and NH_4Cl was identified using spectroscopic remote sensing[40].

The ions in surface salts can provide insights into the origin and evolution of Ganymede and help constrain the nature of subsurface liquid water. As on Earth, Enceladus, Europa and Ceres, the presence of Na at specific locations is indicative of the interaction between liquid water and rocky material[9,39]. This interaction may have occurred early in Ganymede's history when accreted ice–rock mixtures experienced ice melting, and water and other primordial volatiles separated from rocks[41]. Water–rock interaction could have also occurred later if a subsurface ocean was in direct contact with Ganymede's rocky interior when the subsurface heat flow was larger than it is today, or, more recently, if high-pressure ice existing beneath an ocean experienced melting at the surface of the rocky interior[42].

The presence of Cl in salts on Ganymede is easy to explain, as it is likely that Cl was present as a constituent in primordial rocks. Potential chondritic analogues (for example, CI and CM chondrites) of Ganymede's initial rock component contain Cl in relatively high abundances[43], and rocky worlds (for example, Io, Mars and Earth) have significant inventories of Cl (ref. 44). During water–rock separation, as described previously, Cl is leached from rock with high efficiency owing to its hydrophilic nature[45]. It is possible that Cl could also have been accreted as a constituent in primordial ice, such as hydrates of HCl or NH_4Cl formed from the reaction of HCl with NH_3 in cometary ice.

The potential presence of NH_4-bearing salts suggests that Ganymede accreted icy materials that were cold enough to condense ammonia. Ultraviolet spectroscopy data obtained on Ganymede during the same Juno flyby are also consistent with an ammonia-like contaminant at low latitudes[46]. Ammonium salts are likely to be widespread among comets[47], and other planetary bodies located beyond the snow line (for example, Ceres, Enceladus, Titan and Pluto) show evidence of NH_3 or NH_4^+-bearing materials[48–50]. Direct accretion of these species seems to provide the simplest explanation for the inferred presence of NH_4-bearing salts on Ganymede. A more complex and perhaps less likely origin scenario for NH_4^+ would involve hydrothermal processing of N in chondritic insoluble organic matter[51]. The viability of this hypothesis would depend on the conditions being sufficiently reduced and not too hot in Ganymede's rocky interior (otherwise, N_2 would be generated instead[52]). In addition, the apparent absence of nitrates may suggest limited oxidation of ammonium to nitrate if ammonium salts are present.

The origin of carbonate species (including surface CO_2 if endogenic) is likely analogous to that of ammonium ions. That is, the most plausible scenario may involve accretion of volatile-bearing ice, containing CO_2 in this case. Observations of comets show that they contain more CO_2 than NH_3[53]. Some chondrite parent bodies also accreted CO_2, as evidenced by the enrichment of ^{13}C in carbonate minerals[54]. The case of chondritic rock inheritance or one that reflects an additional cometary ice inheritance likely leads to the accretion of CO_2 on Ganymede. This primordial CO_2 could then produce $NaHCO_3$ by rock weathering reactions (see above), or $(NH_4)_2CO_3$ could be produced by the reaction of NH_3 with CO_2 in melted primordial ice. Metamorphism of accreted organic matter mixed with hydrated and oxidized minerals in Ganymede's initial rocky interior could provide an alternative or complementary source of CO_2[55]. Certainly, high temperatures that favour carbon oxidation would have been reached; otherwise, Ganymede would not have a metal core[56].

https://doi.org/10.1038/s41550-023-02107-5

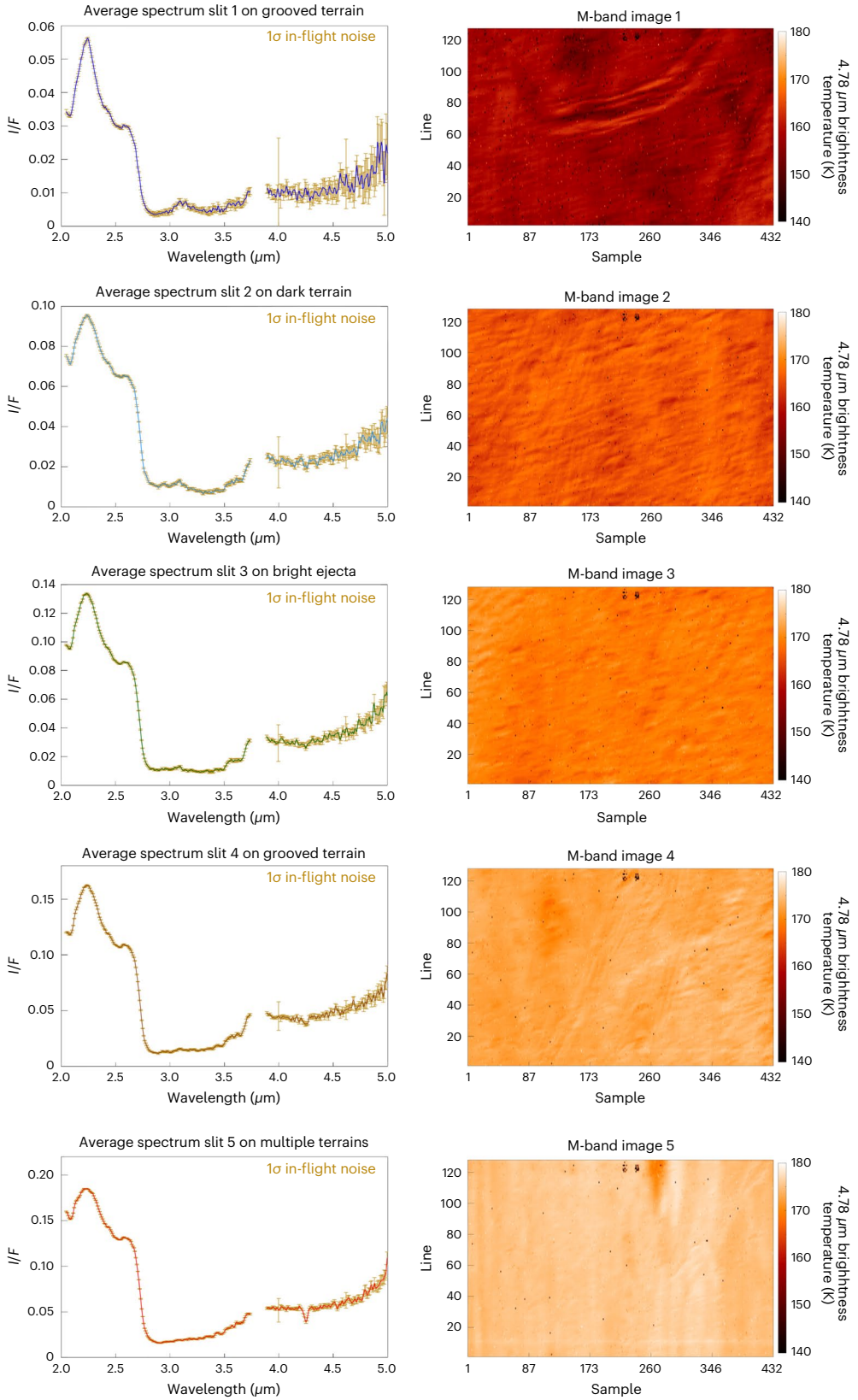

Fig. 2 | Spectral variability in the JIRAM data. Average spectral profiles of Ganymede measured in five separate JIRAM slits. Data are presented as mean values of 159, 241, 241, 241 and 237 pixels, respectively, ± s.e.m. measured on the sky background during the same observation sequence (Methods). Each plot in the left column is named after the terrain unit described in the main text and shown in Supplementary Fig. 13. In the right column, we show the images acquired simultaneously with the JIRAM M-band imaging subsystem, where the colour code is related to the brightness temperature computed at 4.78 μm. All images are 432 × 128 pixels in size. The *x* axis ('sample') identifies the column index, while the *y* axis ('line') identifies the row index. Although smeared, the JIRAM images display geological features in the observed scene, which supports the variability observed in the spectroscopic data.

https://doi.org/10.1038/s41550-023-02107-5

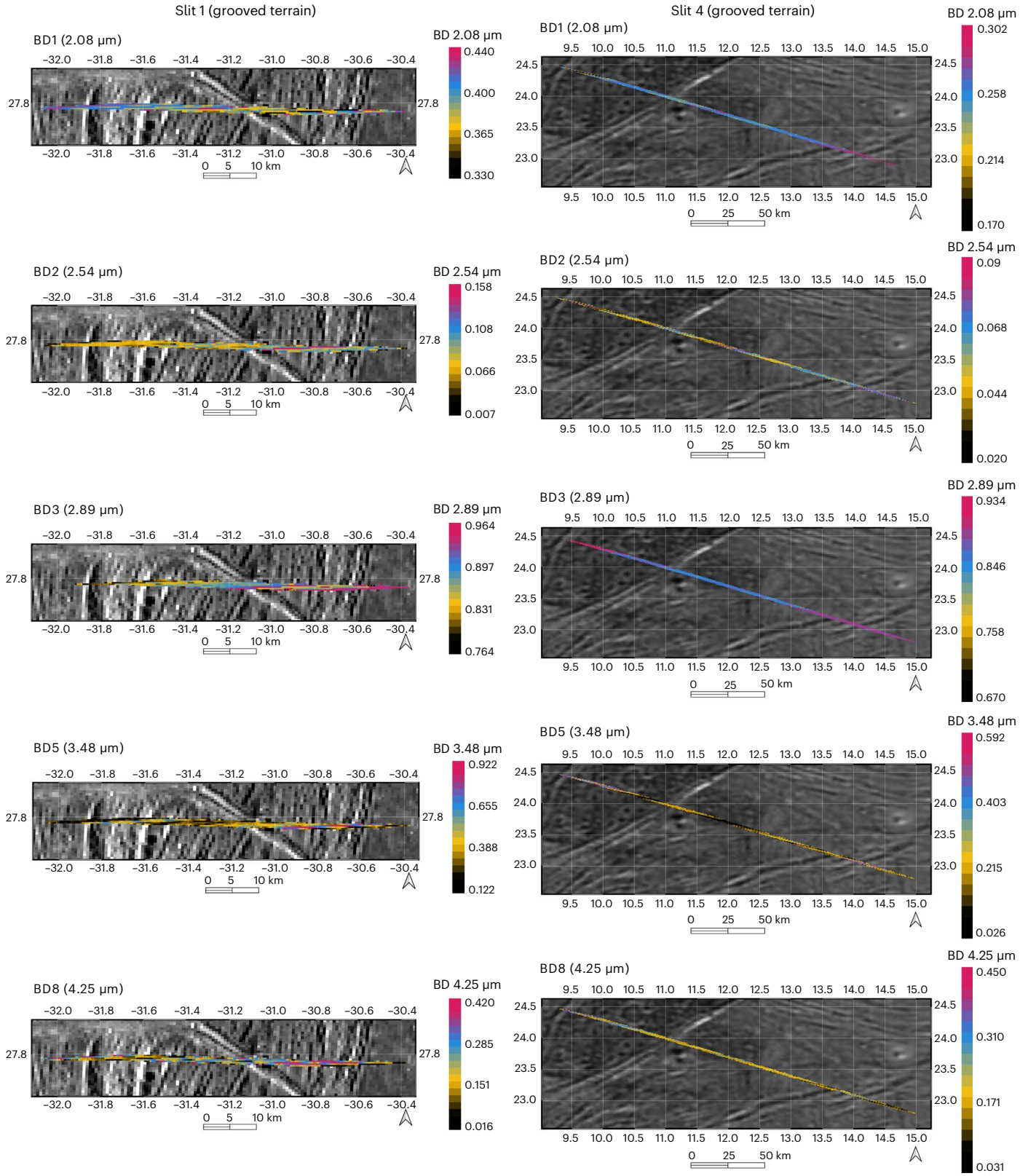

Fig. 3 | Spatial distribution of band strengths in grooved terrains. Closeups of the ground footprints of JIRAM spectral slits 1 (left column) and 4 (right column), covering different grooved terrains. From top to bottom, each panel displays the depth of selected spectral features: 2.08 μm, 2.54 μm, 2.89 μm, 3.48 μm, and 4.25 μm. The labels on the axes express east longitude (x-axis) and north latitude (y-axis). Smearing is accounted for in projecting the ground footprints (Methods). The colours in the projected footprints highlight variability in the observed scene, linked to the composition of the terrains that JIRAM investigated. To allow correlation with geologic features, a JunoCam optical image is used as a background in slit 1 (~1 km/px) (Supplementary Data), while the Voyager+Galileo optical basemap (1 km per pixel)[65] is used in slit 4. A scale bar indicates the size of the observed features. To emphasize band depth values, different stretches are applied in the colorbars of slit 1 and slit 4. The full set of projections for the band depths of all 8 spectral signatures is shown in Supplementary Fig. 14.

https://doi.org/10.1038/s41550-023-02107-5

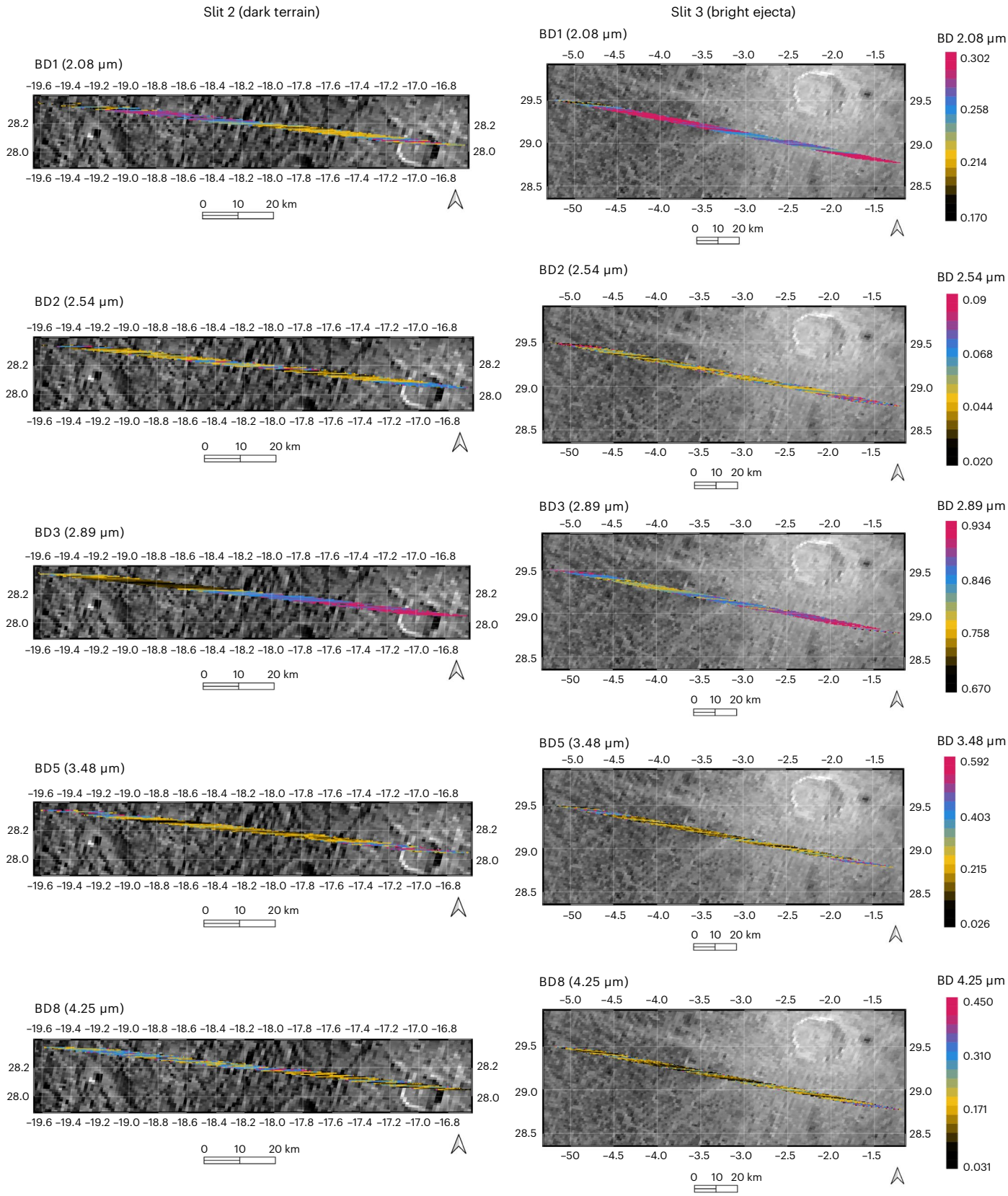

Fig. 4 | Spatial distribution of band strengths in dark and bright terrains. Closeups of the ground footprints of JIRAM spectral slits 2 (left column) and 3 (right column), covering a dark terrain and the bright ejecta of a fresh crater, respectively. The meaning of the panels in terms of band depths, the coordinate system and the projection method are the same as in Figure 3. To allow correlation with geologic features, JunoCam optical images are used as a background (~1 km/px) (Supplementary Data). For each row of panels, the same colorbar applies. The full set of projections for the band depths of all 8 spectral signatures is shown in Supplementary Fig. 14.

https://doi.org/10.1038/s41550-023-02107-5

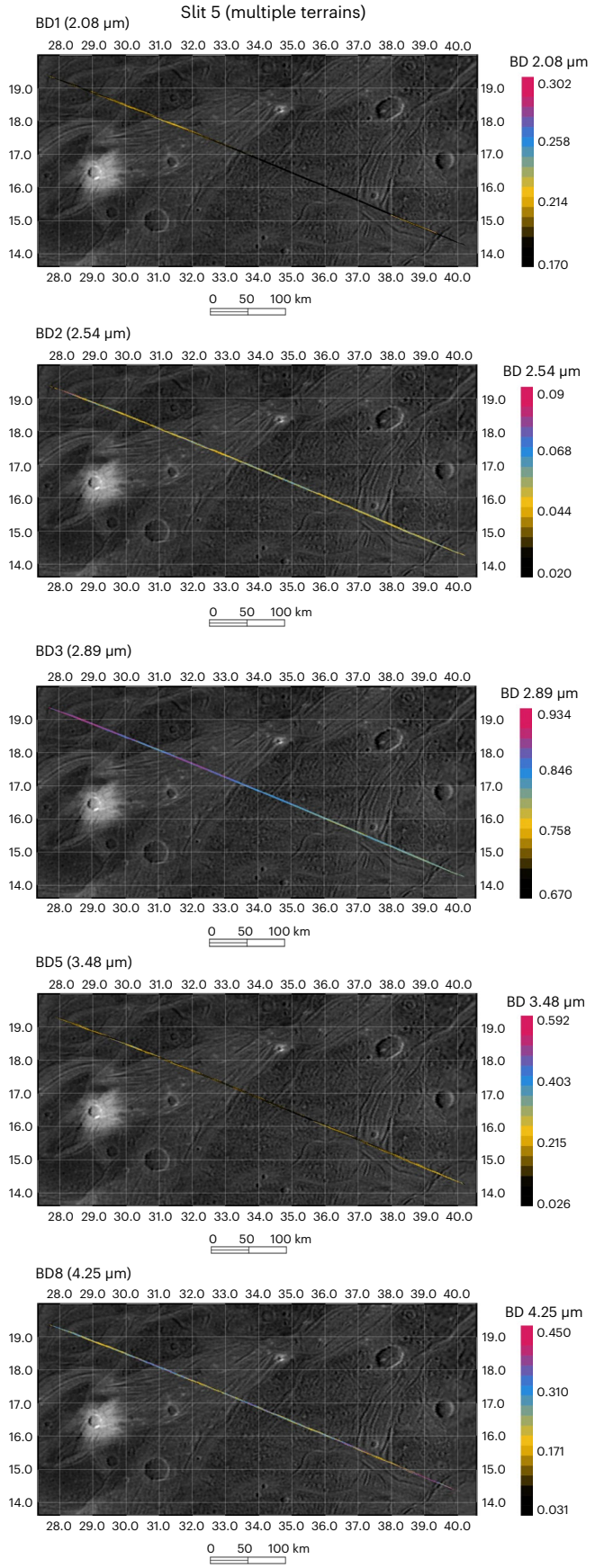

Fig. 5 | Spatial distribution of band strengths in multiple terrains. Closeups of the ground footprints of JIRAM spectral slit 5, covering multiple terrain types including dark terrains and grooved terrains. The meaning of the panels in terms of band depths, the coordinate system and the projection method are the same as in Figure 3 and Figure 4. To allow correlation with geologic features, the Voyager+Galileo optical basemap (1 km px^{-1})[65] is used. The full set of projections for the band depths of all 8 spectral signatures is shown in Supplementary Fig. 14.

Some of the tentatively identified salts are pH-sensitive; therefore, their presence would constrain the pH of the source fluid. Modelling suggests that the source fluid would have been circumneutral to moderately alkaline (Methods). This inference suggests a balance between the acidity produced by volatiles (for example, carbonic acid derived from CO_2) and the basicity inherent to silicate minerals. Extensive water–rock interaction could achieve such a balance and would also be consistent with the presence of sodium salts as an independent indicator of aqueous alteration inside Ganymede.

The salt minerals and organic compounds spectroscopically identified by JIRAM on Ganymede, and their relationship with the geological characteristics of the explored area, suggest that these may be the result of extensive aqueous alteration of silicates that occurred at some point in the history of the satellite, perhaps combined with hydrothermal activity at its depths.

Methods

JIRAM data acquired on Ganymede during orbit 34

In Juno orbit 34, during the close flyby of Ganymede that occurred on 7 June 2021, JIRAM acquired a total of six images and 23 spectral slits. Spectral slits 12–17 were acquired on the day side of Ganymede (Supplementary Fig. 2). We discarded slit 12, the first day side slit, due to poor (grazing) solar illumination resulting in a very low signal-to-noise ratio, whereas the other five slits were retained for scientific analysis. In Table 1 and the main text, for simplicity, we refer to these five slits as slits 1–5.

Each JIRAM slit is composed of 256 spectra, resulting in more than 1,100 individual infrared spectra after filtering only the data with favourable solar illumination and observation conditions (solar incidence angle and emission angle <75°) and ruling out data affected by permanent instrumental artefacts. This spectroscopic dataset was corrected for stray light from Ganymede entering the JIRAM instrument, which added extra signal in the 2.0–3.8 μm wavelength range (see next subsection).

Removal of stray light from the JIRAM spectroscopic data

The JIRAM data acquired soon after the science data discussed in this paper (spectral slit 18 taken at UTC 16:59:57) observed sky background with Ganymede outside the FoV, so it should represent only the thermal background signal of the JIRAM spectrometer. On the contrary, a substantial extra signal appears at short wavelengths, with a flat shape in uncalibrated (raw) data between 2.0 and 3.5 μm, which is different from the usual shape seen in other JIRAM slits of Ganymede as observed by JIRAM (Supplementary Fig. 1). Because this was not observed in any other JIRAM spectral data of the Galilean satellites and all other JIRAM functional parameters were nominal, we deduce that this extra signal is stray light. This stray light did not appear in previous observations of Jupiter or its satellites, which were not as close as this Ganymede flyby, suggesting that the distance from the target and the peculiar geometry of the flyby were largely responsible for its occurrence.

The flat shape of the stray light between 2.0 and 3.5 μm can be explained by the signal coming from the day side of Ganymede, which entered the JIRAM spectrometer's box and reached the focal plane without being dispersed by the grating. A junction between two segments of an order-sorting filter placed on top of the focal plane, whose spectral counterpart is centred at ~3.8 μm (ref. 10), provides a very effective rejection of this stray light, which is not detected between 4.0 and 5.0 μm.

Among the possible ways of removing stray light, we preferred using raw data rather than calibrating the stray light itself and then removing it from the calibrated spectra, as the latter approach induces

spurious signatures due to the instrument transfer function. Therefore, we fitted the stray light of slit 18, averaged over all 256 spatial pixels (samples), with a sigmoid function (Supplementary Fig. 1). However, because the intensity of stray light changes over time as a consequence of Juno/JIRAM moving with respect to Ganymede, before removing the stray light spectrum, this needs to be further corrected for a normalizing factor, whose value changes from slit 13 to slit 17.

The JIRAM L-band imaging subsystem (measuring spectral radiance integrated from 3.3 to 3.6 μm) took images of the surface of Ganymede at the same time as the JIRAM spectrometer. The L-band imager has 432 columns (samples) and 128 rows (lines). Samples/columns from 87 to 342 were located just above the spectrometer slit (with an angular separation of approximately 0.1° between the slit and L-filter border). Because the spatial resolution of these acquisitions is high, we can safely assume that the L-band imager (lines 1–128; samples 87–342; 256 samples in all) and spectrometer slit (256 samples) receive the same physical signal when integrated over a ~3.5° region that is much larger than the angular separation between them. In Supplementary Fig. 2, we show, for each acquisition, the difference between the radiance integrated from 3.3 to 3.6 μm using the spectrometer (R_S) and the radiance collected by the L-band imager (R_L), averaged over the pixels defined previously.

For each acquisition and for each spectrum in the slit, we subtracted a stray light spectrum equal to $k \times R_N$ from the acquired data, where R_N is the calibrated sigmoid function best fitting the average stray light in the raw data, and k is the difference between R_S and R_L, as presented in Supplementary Fig. 2.

Finally, once the spurious signal radiance has been subtracted individually from each of the five spectral slits acquired by JIRAM, the resulting average spectral profile of Ganymede displays a change both in the absolute level of the continuum at the short wavelengths and in the spectral slope between 2.8 and 3.7 μm (Supplementary Fig. 3).

Computation of uncertainties in *I*/*F* spectral profiles

The error bars in Figs. 1b and 2 were derived from the in-flight Noise-Equivalent Spectral Radiance (NESR) measured on the sky background observed by the JIRAM spectrometer, along with observations of Ganymede. We calculated the NESR profile as the standard deviation of the spectral radiance in the sky background pixels of slit 18, that is, the first slit that had Ganymede outside the FoV soon after acquiring the scientific data. A standard error of the mean (s.e.m.) for the NESR can be obtained by assuming that, while averaging over a population of n samples (in our case, n independent spectra of Ganymede), the uncertainty decreases with the square root of n, where n varies from one observation to another (159 spectra per pixel for slit 1; 241 for slits 2, 3 and 4; and 237 spectra per pixel for slit 5, or 1,179 spectra per pixel for the entire dataset shown in Fig. 1b). Finally, for each spectral profile, the NESR s.e.m. was converted into *I*/*F* units by dividing it by the solar radiance scaled by the heliocentric distance at the time of observation (5.051 au). Consistent with previous studies based on JIRAM spectroscopic data, we referred to the high-resolution Moderate Resolution Transmission (MODTRAN) Cebula+Kurucz extraterrestrial solar spectrum[57], convolved for the response of the individual spectral channels of the JIRAM spectrometer[58].

Computation of BDs and associated uncertainties

For each of the eight spectral signatures highlighted in Fig. 1b, the calculation of BDs was performed by first removing the spectral continuum by means of a linear fit between the shoulders of the bands, and then evaluating the depth[59] as $BD = (R_C - R_B)/R_C$, where R_B and R_C are the reflectance at the band centre and the reflectance of the spectral continuum at the band centre, respectively. To calculate the uncertainty associated with the BD of the main spectral signatures displayed in the average spectrum of Fig. 1b, we considered the mean in-flight noise in units of *I*/*F* discussed in the previous subsection and applied error propagation to calculate the absolute uncertainty ΔBD associated with a given BD (that is, the uncertainty associated with the ratio R_B/R_C, given by R_B/R_C multiplied by the sum of the relative errors on R_B and R_C), and hence the ratio between BD and associated uncertainty. The value of this ratio can be used to discriminate between the 'strong' and 'weak' absorption bands. The details regarding these parameters are specified in Supplementary Table 1.

Plots of different material categories

In Supplementary Figs. 4–11, stacked plots in the 2–5 μm range are shown for the following categories of endogenous compounds: water ice, chlorides, carbonates, sulfates, nitrates and phyllosilicates (smectites). We also present a stacked plot for organics and some exogenous products displaying diagnostic features in the near-infrared range. In each stacked plot, we compared the average spectral profile of Ganymede as measured by JIRAM in *I*/*F* units with the reflectance profiles of different compounds measured in the laboratory after convolution for the JIRAM spectral resolution[58]. Measurements at cryogenic temperatures, if available, were preferred over those at room temperatures. When multiple grain sizes were available, we chose coarse-grained compounds because at the low latitudes investigated by JIRAM, water ice is coarse-grained[4,26]. The black, thick dashed lines mark the wavelength positions of the main absorptions revealed by JIRAM (located at 2.08, 2.54, 2.89, 3.00, 3.48, 3.58, 3.65 and 4.25 μm), whereas thinner, goldenrod dashed lines mark the positions of weaker features (at 2.22, 2.42, 2.60, 2.82, 3.05, 3.16, 3.25 and 3.38 μm).

Spectral unmixing

We applied linear spectral unmixing to the JIRAM data, both to the global average spectrum of Ganymede and separately for each of the five slits covering different terrain types, using two consolidated approaches: fully constrained least squares (FCLS) and Markov chain Monte Carlo (MCMC). FCLS is a linear minimization algorithm[60]. MCMC is a statistical sampling method that uses Markov chains to generate samples from a desired probability distribution[61].

We first set up a library from the laboratory spectral profiles of compounds relevant to the surface composition of Ganymede, as found in the literature (Supplementary Table 2). All profiles were convolved to match the JIRAM spectral resolution[58]. We initially applied FCLS modelling to individual categories of compounds (that is, chlorides, sulfates, carbonates, nitrates, smectites, organics and exogenic species) to evaluate which compound within each category provides the best fit (that is, the minimum χ^2 value) to JIRAM data in the 2.0–3.7 μm region shortward of the filter gap. We then considered the best candidate in each category and reran the model using a mixture of all the best candidates. Coarse-grained water ice was always included among the spectral endmembers. Two synthetic, spectrally flat endmembers with constant value of 1.0 and 0.0 (respectively tagged 'white' and 'black') were used to model the albedo, as done in other recent studies (for example, ref. 26). In the second step, we applied MCMC to validate the results obtained using FCLS. To facilitate numerical convergence within a reasonable processing time while maintaining a close approximation to JIRAM data, we enforced a spectral correlation length of 20 nm, which means that different wavelengths are highly correlated at this spectral scale (corresponding to roughly two JIRAM spectral channels). The results are presented in Supplementary Fig. 15.

The general observation is that, although these unmixing models can properly fit the spectral continuum, they can hardly reproduce specific weak and/or narrow spectral signatures. Furthermore, no substantial percentages of water ice are needed to return a good fit, because several hydrates mimic the spectral profile of water ice in the region between 2 and 3 μm. When using MCMC, the coefficients of the linear combination associated with hydrated sulfuric acid are substantially higher than in the case of FCLS; however, the best fit in

general improves by excluding this compound, for which no reflectance spectral profiles measured in the laboratory exist longward of 2.5 µm.

Reconstruction of geometric information for the JIRAM spectroscopic data

The computation of geometric information for the JIRAM data is typically obtained using the SPICE toolkit[62]. However, in this specific close Ganymede flyby, the SPICE-derived geometric information shows substantial deviations from the observed data, which are due to the large relative speed of the spacecraft and are highlighted by known surface features or an offset in the limb profile of Ganymede. Hence, to improve the SPICE-based geometric information for JIRAM, we applied a limb-fitting technique similar to that used in another study[13].

First, geometric information for JunoCam optical images (106*xx*-Metadata.json, with *xx* ranging from 29 to 32) was computed using SPICE, and the geometric values were adjusted by fitting the limb of Ganymede. By comparing the location and shape of the surface features observed in the JunoCam images with those observed in the JIRAM images, we derived the geometric information of the JIRAM spectral data consequently, because the relative alignment of the JIRAM spectrometer and the JIRAM double imager is known to have very high accuracy (<1 pixel[58]). To take smearing into account, the geometric information concerning the latitude and longitude of the JIRAM spectroscopic data is calculated not only for the pixel centre but also for the four corners of each pixel, both at the beginning and end of the exposure. This way, for each pixel, we obtain a projected trapezoid that represents the effective area covered during the exposure time.

To finally map the JIRAM data, we considered for each spectral slit a grid with fixed angular resolution matching the nominal pixel resolution, ranging from 0.31 km per pixel (slit 1) to 0.61 km per pixel (slit 5). Starting from the knowledge of the individual JIRAM ground footprints/trapezoids, we sum all BD values falling within a given angular bin and then average the data keeping track of the overall redundancy. This approach ultimately allowed us to properly map each of the five JIRAM spectral slits despite the variable spatial resolution.

Correlation coefficients for pairs of BDs

To evaluate potential correlations in surface composition, as observed by JIRAM, we calculated the correlation coefficients between the depths of the eight main spectral features shown in Fig. 1b. Because JIRAM's spectral slits sample different terrain types, to properly evaluate correlations arising among different spectral signatures, we produced one correlation matrix for each slit to highlight different behaviours from one region to another, rather than mixing all BD values together (Supplementary Table 3). In all slits, no systematic correlations arose between any pair of spectral signatures, which could point to systematic instrumental artefacts/residuals.

Geochemical interpretations of inferred salt compositions

We performed thermodynamic calculations using the code SUPCRTBL[63] to quantify how relative abundances in the CO_2–HCO_3^-–CO_3^{2-} and NH_4^+–NH_3 systems would change as a function of pH. These calculations are approximate because they correspond to 0 °C and 1 bar, and ionic strength effects are neglected. The source fluid may actually chemical speciate as a brine that is at subzero temperatures before salt deposition. However, we consider our simplified systems to be appropriate given the nature of the current observational data (that is, inferred presence of a few salts rather than detailed concentration information). In addition, low pressure is appropriate for the source fluid when it is in the shallow subsurface before extrusion. We hold an agnostic view as to how the source fluid considered here could relate to a salty water ocean that resides inside Ganymede[2].

Supplementary Fig. 16 quantifies the pH dependence of the speciation of ammonia and carbonate species. This figure allows us to constrain the pH to be consistent with the composition of salts inferred from the JIRAM data. Supplementary Table 4 provides the suggested constraints on pH for the indicated salt to have a 'significant' abundance. Significance is treated subjectively here based on Supplementary Fig. 16, as the observational data are qualitative with regard to how they constrain aqueous chemistry. Nevertheless, pH operates over a log scale, which helps mitigate this type of uncertainty. It is not straightforward to interpret Supplementary Fig. 16 for $(NH_4)_2CO_3$ because the figure treats the two speciation systems separately, while they are clearly linked in the case of this compound. We clarified this issue by performing a coupled speciation calculation for $(NH_4)_2CO_3$ using The Geochemist's Workbench and obtained a pH of ~10.

We conclude that a salt assemblage on Ganymede's surface that includes significant $NaHCO_3$ should have a source fluid pH between ~6 and ~11, while an alternative assemblage containing a significant amount of $(NH_4)_2CO_3$ would probably require a pH close to 10. Both endmembers would be consistent with the coexistence of NH_4Cl and $NaCl{\cdot}2H_2O$. It appears that the source fluid would have been circumneutral to moderately alkaline. This inference suggests a balance between the acidity produced by volatiles (for example, carbonic acid derived from CO_2) and the basicity that is inherent to silicate minerals.

Data availability

The JIRAM dataset used for our analysis is publicly available at the Juno Archive of the Planetary Atmospheres Node (https://pds-atmospheres.nmsu.edu/PDS/data/PDS4/juno_jiram_bundle/data_calibrated/orbit34/). The filenames of the JIRAM spectroscopic data for Ganymede are listed in Table 1. Source data are provided with this paper[64].

Code availability

The computer code used to produce *I*/*F* spectral profiles of Ganymede and to compute band depths is a direct implementation of the procedures described in the Methods section. Spectral unmixing with FCLS was carried out using PySptools, available at https://pysptools.sourceforge.io/. Spectral unmixing with MCMC is a direct implementation of the algorithm[61]. The computer code used to model the chemical speciation of NH_3 and CO_2 is a direct implementation of the SUPCRTBL code[63].

References

1. Schenk, P. M. Thickness constraints on the icy shells of the Galilean satellites from a comparison of crater shapes. *Nature* **417**, 419–421 (2002).
2. Saur, J. et al. The search for a subsurface ocean in Ganymede with Hubble Space Telescope observations of its auroral ovals. *J. Geophys. Res. Space Phys.* **120**, 1715–1737 (2015).
3. Carlson, R. W. et al. Near-infrared mapping spectrometer experiment on Galileo. *Space Sci. Rev.* **60**, 457–502 (1992).
4. Stephan, K., Hibbitts, C. A. & Jaumann, R. H_2O-ice particle size variations across Ganymede's and Callisto's surface. *Icarus* **337**, 113440 (2020).
5. McCord, T. B. et al. Hydrated salt minerals on Ganymede's surface: evidence of an ocean below. *Science* **292**, 1523–1525 (2001).
6. McCord, T. B. et al. Hydrated salt minerals on Europa's surface from the Galileo near-infrared mapping spectrometer (NIMS) investigation. *J. Geophys. Res.* **104**, 11827–11852 (1999).
7. Ligier, N. et al. VLT/SINFONI observations of Europa: new insights into the surface composition. *Astron. J.* **151**, 163 (2016).
8. Ligier, N. et al. Surface composition and properties of Ganymede: updates from ground-based observations with the near-infrared imaging spectrometer SINFONI/VLT/ESO. *Icarus* **333**, 496–515 (2019).
9. Trumbo, S. K., Brown, M. E. & Hand, K. P. Sodium chloride on the surface of Europa. *Sci. Adv.* **5**, aaw7123 (2019).
10. Adriani, A. et al. JIRAM, the Jovian Infrared Auroral Mapper. *Space Sci. Rev.* **213**, 393–446 (2017).

11. Bolton, S. J. et al. The Juno mission. *Science* **356**, 821–825 (2017).
12. Hansen, C. J. et al. Juno's close encounter with Ganymede—An overview. *Geophys. Res. Lett.* **49**, e2022GL099285 (2022).
13. Mura, A. et al. Infrared observations of Ganymede from the Jovian InfraRed Auroral Mapper on Juno. *J. Geophys. Res. Planets* **125**, e2020JE006508 (2020).
14. Wang, F. et al. Laboratory and field characterization of visible to near-infrared spectral reflectance of nitrate minerals from the Atacama Desert, Chile, and implications for Mars. *Am. Mineral.* **103**, 197–206 (2018).
15. De Angelis, S. et al. High temperature VIS-IR Spectroscopy of NH_4 phyllosilicates. *J. Geophys. Res. Planets* **126**, e06696 (2021).
16. Berg, B. L. et al. Reflectance spectroscopy (0.35–8 μm) of ammonium-bearing minerals and qualitative comparison to Ceres-like asteroids. *Icarus* **265**, 218–237 (2016).
17. Ehlmann, B. L. et al. Ambient and cold-temperature infrared spectra and XRD patterns of ammoniated phyllosilicates and carbonaceous chondrite meteorites relevant to Ceres and other solar system bodies. *Meteorit. Planet. Sci.* **53**, 1884–1901 (2018).
18. Mastrapa, R. M. et al. Optical constants of amorphous and crystalline H_2O-ice: 2.5–22 μm (4000–455 cm^{-1}) optical constants of H_2O-ice. *Astrophys. J.* **701**, 1347–1356 (2009).
19. McCord, T. B. et al. Organics and other molecules in the surfaces of Callisto and Ganymede. *Science* **278**, 271–275 (1997).
20. Socrates, G. *Infrared and Raman Characteristic Group Frequencies: Tables and Charts* (John Wiley & Sons, 2004); https://isbnsearch.org/isbn/978-0-470-09307-8
21. Moroz, L. V. et al. Natural solid bitumens as possible analogs for cometary and asteroid organics: 1. Reflectance spectroscopy of pure bitumens. *Icarus* **134**, 253–268 (1998).
22. Ciarniello, M. et al. VIS-IR spectroscopy of mixtures of water ice, organic matter, and opaque mineral in support of small body remote sensing observations. *Minerals* **11**, 1222 (2021).
23. Chaban, G. M. et al. Carbon dioxide on planetary bodies: theoretical and experimental studies of molecular complexes. *Icarus* **187**, 592–599 (2007).
24. Carlson, R. W. et al. Hydrogen peroxide on the surface of Europa. *Science* **283**, 2062–2064 (1999).
25. Carlson, R. W., Johnson, R. E. & Anderson, M. S. Sulfuric acid on Europa and the radiolytic sulfur cycle. *Science* **286**, 97–99 (1999).
26. King, O. & Fletcher, L. N. Global modelling of Ganymede's surface composition: near-IR mapping from VLT/SPHERE. *J. Geophys. Res. Planets* **127**, e2022JE007323 (2022).
27. Trumbo, S. K. et al. Hydrogen peroxide at the poles of Ganymede. *Sci. Adv.* **9**, eadg3724 (2023).
28. Nash, D. B. & Betts, B. H. Laboratory infrared spectra (2.3–23 μm) of SO_2 phases: applications to Io surface analysis. *Icarus* **117**, 402–419 (1995).
29. Douté, S. et al. Mapping SO_2 frost on Io by the modeling of NIMS hyperspectral images. *Icarus* **149**, 107–132 (2001).
30. Hibbitts, C. A., McCord, T. B. & Hansen, G. B. Distributions of CO_2 and SO_2 on the surface of Callisto. *J. Geophys. Res.* **105**, 22,541–22,557 (2000).
31. Collins, G. C. et al. *Global geologic map of Ganymede*: *Scientific Investigations Map 3237* (US Geological Survey, 2013); https://doi.org/10.3133/sim3237
32. Hibbitts, C. A. et al. Carbon dioxide on Ganymede. *J. Geophys. Res.* **108**, 5036–5058 (2003).
33. Aponte, J. C. et al. Analyses of aliphatic aldehydes and ketones in carbonaceous chondrites. *ACS Earth Space Chem.* **3**, 463–472 (2019).
34. Khawaja, N. et al. Low-mass nitrogen-, oxygen-bearing, and aromatic compounds in Enceladean ice grains. *Mon. Not. R. Astron. Soc.* **489**, 5231–5243 (2019).
35. Grossmann, Y. et al. Aliphatic aldehydes in the Earth's crust—Remains of prebiotic chemistry? *Life* **12**, 925 (2022).
36. Liuzzo, L. et al. Variability in the energetic electron bombardment of Ganymede. *J. Geophys. Res. Space Phys.* **125**, e28347 (2020).
37. Poppe, A. R. et al. Thermal and energetic ion dynamics in Ganymede's magnetosphere. *J. Geophys. Res. Space Phys.* **123**, 4614–4637 (2018).
38. Plainaki, C. et al. Kinetic simulations of the Jovian energetic ion circulation around Ganymede. *Astrophys. J.* **900**, 74 (2020).
39. Postberg, F. et al. Sodium salts in E-ring ice grains from an ocean below the surface of Enceladus. *Nature* **459**, 1098–1101 (2009).
40. De Sanctis, M. C. et al. Fresh emplacement of hydrated sodium chloride on Ceres from ascending salty fluids. *Nat. Astron.* **4**, 786–793 (2020).
41. Kirk, R. L. & Stevenson, D. J. Thermal evolution of a differentiated Ganymede and implications for surface features. *Icarus* **69**, 91–134 (1987).
42. Kalousová, K. et al. Two-phase convection in Ganymede's high-pressure ice layer—Implications for its geological evolution. *Icarus* **299**, 133–147 (2018).
43. Sharp, Z. D. et al. The chlorine isotope composition of chondrites and Earth. *Geochim. Cosmochim. Acta* **107**, 189–204 (2013).
44. Lellouch, E. et al. Volcanically emitted sodium chloride as a source for Io's neutral clouds and plasma torus. *Nature* **421**, 45–47 (2003).
45. Glein, C. R. & Shock, E. L. Sodium chloride as a geophysical probe of a subsurface ocean on Enceladus. *Geophys. Res. Lett.* **37**, L09204 (2010).
46. Molyneux, P. M. et al. Ganymede's UV reflectance from Juno-UVS data. *Geophys. Res. Lett.* **49**, e2022GL099532 (2022).
47. Poch, O. et al. Ammonium salts are a reservoir of nitrogen on a cometary nucleus and possibly on some asteroids. *Science* **367**, eaaw7462 (2020).
48. De Sanctis, M. C. et al. Ammoniated phyllosilicates with a likely outer Solar System origin on (1) Ceres. *Nature* **528**, 241–244 (2015).
49. Waite, J. H. et al. Cassini finds molecular hydrogen in the Enceladus plume: evidence for hydrothermal processes. *Science* **356**, 155–159 (2017).
50. Mandt, K. E. et al. Protosolar ammonia as the unique source of Titan's nitrogen. *Astrophys. J. Lett.* **788**, L24 (2014).
51. Pizzarello, S. & Williams, L. B. Ammonia in the early Solar System: an account from carbonaceous chondrites. *Astrophys. J.* **749**, 161 (2012).
52. Miller, K. E. et al. Contributions from organic nitrogen to Titan's N_2 atmosphere: new insights from cometary and chondritic data. *Astrophys. J.* **871**, 59 (2019).
53. Dello Russo, N. et al. Emerging trends and a comet taxonomy based on the volatile chemistry measured in thirty comets with high-resolution infrared spectroscopy between 1997 and 2013. *Icarus* **278**, 301–332 (2016).
54. Fujiya, W. et al. Migration of D-type asteroids from the outer Solar System inferred from carbonate in meteorites. *Nat. Astron.* **3**, 910–915 (2019).
55. Melwani Daswani, M. et al. A metamorphic origin for Europa's ocean. *Geophys. Res. Lett.* **48**, e2021GL094143 (2021).
56. Gomez Casajus, L. et al. Gravity field of Ganymede after the Juno Extended Mission. *Geophys. Res. Lett.* **49**, e2022GL099475 (2022).
57. MODTRAN extraterrestrial solar irradiance (National Renewable Energy Laboratory) https://www.nrel.gov/grid/solar-resource/spectra.html#paneld10e138_1

58. Adriani, A. et al. Juno's Earth flyby: the Jovian InfraRed Auroral Mapper preliminary results. *Astrophys. Space Sci.* **361**, 272 (2016).
59. Clark, R. N. & Roush, T. L. Reflectance spectroscopy: quantitative analysis techniques for remote sensing applications. *J. Geophys. Res.* **89**, 6329–6340 (1984).
60. Heinz D., Chang C.-I. & Althouse, M. Fully constrained least-squares based linear unmixing. In *IEEE 1999 International Geoscience and Remote Sensing Symposium* (Ed. Stein, T. I.) 1401–1403 (1999); https://doi.org/10.1109/IGARSS.1999.774644
61. Spade, D. A. in *Principles and Methods for Data Science Vol. 43* (eds Srinivasa Rao, A. S. R. and Rao, C. R.) 1–66 (Elsevier North-Holland, 2020).
62. Acton, C. H. et al. A look towards the future in the handling of space science mission geometry. *Planet. Space Sci.* **150**, 9–12 (2018).
63. Zimmer, K. et al. SUPCRTBL: a revised and extended thermodynamic dataset and software package of SUPCRT92. *Comput. Geosci.* **90**, 97–111 (2016).
64. Tosi, F. Data package for the Nature Astronomy paper: 'Salts and organics on Ganymede's surface from infrared observations by Juno/JIRAM' (Tosi et al.). *figshare* https://doi.org/10.6084/m9.figshare.21710468 (2023).
65. Ganymede Voyager - Galileo SSI Global Mosaic 1km v1. *Annex* https://astrogeology.usgs.gov/search/map/Ganymede/Voyager-Galileo/Ganymede_Voyager_GalileoSSI_global_mosaic_1km (2013).

Acknowledgements

The JIRAM instrument is funded by the Italian Space Agency (Agenzia Spaziale Italiana (ASI)). It was built by Selex ES under the leadership of the Italian National Institute for Astrophysics (Istituto Nazionale di Astrofisica (INAF))–Institute for Space Astrophysics and Planetology (Istituto di Astrofisica e Planetologia Spaziali (IAPS)), Rome, Italy. JIRAM is operated by INAF–IAPS, Rome, Italy. F.T., A. Mura, A. Cofano, F.Z., M.C., G.P., C.P., R.S., A.A., A. Migliorini, L.A., F.A., A. Cicchetti, B.M.D., D.G., A. Moirano, M.L.M., R.N., P.S., G.S., S.S. and D.T. acknowledge the support from the ASI–INAF grant no. 2016-23-H.0 plus addendum no. 2016-23-H.2-2021. C.R.G. was supported in part by the NASA grants NNN13D485T and 80NSSC19K0611. Support for S.J.B. and the Juno project is provided under the NASA grant NNM06AA75C to the Southwest Research Institute. J.I.L. acknowledges support from the Juno mission through subcontract D99069MO from the Southwest Research Institute. C.J.H. acknowledges support from the Juno project through a subcontract from the Southwest Research Institute. T.A.N. was supported by the NASA grant 80NM0018F0612. Support from the Juno Science and Operations Teams is gratefully acknowledged.

Author contributions

F.T. led the analysis and interpretation of the JIRAM data, writing major sections of the main text and Methods. A. Mura is the team leader of the JIRAM instrument; he derived geometric information for the JIRAM data, provided correction for stray light and wrote part of the Methods. A. Cofano searched laboratory spectra available in the literature and relevant for the JIRAM spectral range, highlighting the spectral matches in Extended Data Table 1, and performed spectral unmixing. F.Z. mapped the JIRAM data and contributed to the interpretation. C.R.G. wrote a part of the Discussion and Methods sections. M.C. and G.P. contributed to the discussion of results. J.I.L. and C.P. contributed to the data interpretation. R.S. and A. Cicchetti managed the operation of the JIRAM instrument. R.N. was responsible for the JIRAM calibration pipeline. All authors contributed to the discussion of the results and helped with manuscript preparation.

Competing interests

The authors declare no competing interests.

Additional information

Extended data is available for this paper at https://doi.org/10.1038/s41550-023-02107-5.

Supplementary information The online version contains supplementary material available at https://doi.org/10.1038/s41550-023-02107-5.

Correspondence and requests for materials should be addressed to Federico Tosi.

Peer review information *Nature Astronomy* thanks Paul Hayne and the other, anonymous, reviewer(s) for their contribution to the peer review of this work.

https://doi.org/10.1038/s41550-023-02107-5

Extended Data Table 1 | Chemical compounds relevant to Ganymede surface composition

A	B	C	D	E	F	G	H	I	J	K	L
COMPOUND	MEASURED QUANTITY	2.08 μm	2.54 μm	2.89 μm	3.00 μm	3.48 μm	3.58 μm	3.65 μm	4.25 μm	TOT	Strong spectral features in the range 2–5 μm
VOLATILES											
H2O (water) ice (110 K, 300 μm grain size) 66	R			x						1	2.89 μm
O2 ice (oxygen) (25 K) 95	A									0	3.06 μm
CO2 (carbon dioxide) ice (70 K) 95	A								4.27 μm	1	4.27 μm (but also 2.70 and 2.78 μm)
CH4 (methan) ice (31 K) 96	A									0	3.32 μm
NH3 (ammonia) ice (95 K) 97	A									0	2.95, 2.96 μm
NH3 · H2O (hydrated ammonia) ice (130 K) 97	A									0	2.21, 3.08 μm
SO2 (sulfur dioxide) frost (130K, 2 mm thick) 28	R		x				3.57 μm			2	4.07, 4.38 μm (but also 2.54, 2.79, 3.57, 3.78 μm)
SO2 (sulfur dioxide) frost (125K, from 250 to 500 μm grain size) 29	R		x				3.59 μm			2	4.07 & 4.37 μm (but also 2.54, 2.79, 3.78 μm)
ENDOGENIC PRODUCTS (SALTS)											
NaCl (3B, Nicolet) 67	R	2.09 μm								1	2.96 μm
NaCl · 2H2O (hydrohalite) (100 K) 68	R		2.53 μm	2.91 μm	3.01 μm					3	2.91 μm (but also 2.53, 4.52 μm)
MgCl2 · 2H2O (magnesium dichloride dihydrate) (110 K) 70	R									0	2.00, 2.85, 3.10, 4.50 μm (but also 2.12, 2.38, 2.44, 2.56, 3.90 μm)
MgCl2 · 6H2O (bischofite) (110 K) 70	R		x	2.90 μm						2	2.0 μm (but also vs/sat: 2.3–2.8 H2O combinations/overtones, 3.1–3.7 H2O fundamental stretching region)
CaCl2 (calcium chloride) (flakes >250 μm) 69	R			x	3.01 μm					2	2.89 μm (but also 2.12, 2.46, 2.59, 3.36, 3.96, 4.85 μm)
CaCl2 (calcium chloride) (particles >250 μm) 98	R			x	3.01 μm					2	2.89 μm (but also 2.12, 2.46, 2.59, 3.36, 3.96, 4.63, 4.84 μm)
CaCl2 · 4H2O (80 K, interval 1.1 – 2.7 μm) 99	R	2.09 μm	2.56 μm							2	2.57 μm
CaCl2 · 6H2O (80 K, interval 1.1 – 2.7 μm) 99	R	2.07 μm	2.55 μm							2	2.55 μm (but also 2.47, 2.59, 3.89 μm)
KCl (potassium chloride or sylvite) (77 K, interval 1.4 – 2.6 μm) 100	R									0	
NH4Cl (ammonium chloride) 16	R	x					3.57 μm			1	2.08, 2.20, 3.08, 3.57 μm (but also 2.35, 3.27 μm)
MgSO4 · 6H2O (hexahydrite) (113 K) 75	R				x					1	2.50 & 3.0 μm (but also 2.01, 2.06, 2.12, 2.20, 2.70 μm)
MgSO4 · 7H2O (epsomite) (113 K) 75	R				x					1	2.50 & 3.0 μm (but also 2.0, 2.06, 2.70 μm)
MgSO4 · 11H2O (undecahydrate or meridianiite) (100 K, interval 0.4 – 2.5 μm) 101	R									0	1.99, 2.48 μm (but also 2.05, 2.22, 2.37 μm)
Na2SO4 (sodium sulfate or thénardite) (110 K) 77	R				3.01 μm	x				2	3.01, 4.20, 4.40,4.66 μm (but also 3.10, 3.24, 3.48, 3.68, 3.86 μm)
Na2SO4 · 10H2O (mirabilite) (110 K) 77	R				x					1	1.48, 1.95, 3.0, 4.60 μm (but also 2.47 μm)
Na2Mg(SO4)2 · 4H2O (bloedite) (Nicolet) 78	R	x	2.55 μm	2.87 μm						3	2.87 μm
CaSO4 (anhydrite) (Nicolet) 62	R	x		x		x				3	2.89, 4.69 μm
CaSO4 · 2H2O (gypsum) (150 K) 71	R	2.05 μm		2.87 μm						2	2.05, 2.20, 2.48, 2.87, 4.48 μm
(NH4)2SO4 (ammonium sulfate or mascagnite) 14	R				3.01 μm					1	2.13 & 3.01 & 4.86 μm
NaHCO3 (sodium bicarbonate) 62	R			2.88 μm		x				2	3.36, 3.48 μm (but also 2.03, 4.60 μm)
Na2CO3 (natrite) (113 K) 67	R		x		3.01 μm	3.49 μm				3	3.00, 3.40, 3.49, 3.88, 3.99 μm (but also 2.34, 2.54 μm)
Na2CO3 · 1H2O (thermonatrite) (113 K) 67	R			2.90 μm						1	2.90 & 3.99 μm (but also 2.06, 2.20, 2.50 μm)
Na2CO3 · 10H2O (natron) (113 K) 67	R									0	2.80 & 3.99 μm (but also 2.45 μm)
Na3(CO3)(HCO3)·2(H2O) (trona) 68	R	2.05 μm								1	2.05, 3.13 μm
CaCO3 (calcium carbonate) (interval 0.3 – 3.4 μm, 1530 Specpure CaCO3) 100	R	x	x							2	2.54, 2.80, 3.36 μm (but also 2.34 μm)
CaCO3 (calcite) (Nicolet) 67	R		x	x		x				3	3.98 μm (but also 3.35, 3.48 μm)
CaCO3 · H2O (monohydrocalcite) (interval 0.3 – 2.5 μm) 103	R	x								1	2.08 μm
CaCO3 · 6H2O (ikaite) (interval 0.3 – 2.5 μm) 103	R	2.07 μm								1	2.07 μm
(NH4)2CO3 (ammonium carbonate) 16	R			x						1	3.00 μm (but also 2.17, 2.89 μm)
(NH4)2CO3 (ammonium carbonate) 74	T		x	x		x				3	3.36, 3.48 μm (but also 3.14, 3.90 μm)
NH4NO3 (ammonium nitrate) (120 K) 81	R		2.52 μm		3.02 μm	3.49 μm				3	2.02, 2.14, 3.02, 3.49 μm (but also 4.14, 4.50 μm)
NaNO3 (sodium nitrate) 79	R	2.06 μm		2.87 μm		3.50 μm		x		3	2.62, 2.87, 3.18, 3.50, 3.65, 3.98, 3.74 μm
KNO3 (potassium nitrate) 80	R	2.09 μm		2.91 μm			3.59 μm	x		2	2.91, 3.59, 3.65, 4.17, 4.84 μm
SMECTITES											
Antigorite (Serpentine group) (180 K) 82	R		2.52 μm							1	2.74 μm
Beidellite 83	R		2.52 μm							1	2.72 μm
Chrysotile (Serpentine group) 84	R		2.56 μm							1	2.70 μm
Hectorite 85	R		2.53 μm			3.47 μm				2	2.72 μm
Lizardite (Serpentine group) 67	R		2.56 μm			3.49 μm				2	2.70 μm
Montmorillonite (70 K) 86	R					3.51 μm	3.59 μm			2	2.75 μm
Nontronite 87	R		2.52 μm			3.50 μm				2	2.80 μm
Saponite 88	R									0	2.72 μm
ORGANICS											
IOM (different types) 92	R									0	3.36 μm
Kerogen (PPRG 114) 92	R					x				1	3.41 μm
CH3OH (methanol) (110 K) 104	A									0	3.04, 3.14, 3.53 μm
C2H2 (acetylene) (70 K) 105	T			2.90 μm	x					2	3.09 μm (weaker: 2.45, 2.58, 2.90, 2.94, 3.0 μm)
C2H4 (ethylene) (60 K) 105	T		2.55 μm			x				2	3.23, 3.36 μm
C2H6 (ethane) (80 K) 106	R		x					3.66 μm		2	2.27, 2.31, 2.40, 2.46, 4.96 μm (but also 3.77, 3.91 μm)
C3H8 (propane) (75 K) 106	R		2.55 μm					3.66 μm	4.24 μm	3	4.24, 4.95 μm
C6H6 (benzene) (80 K) 106	R					x		3.66 μm		2	3.23, 3.26, 3.29 μm
C10H8 (naphthalene) (85 K) 67	R					x	3.59 μm	x		3	3.26 μm
C14H10 (anthracene) (85 K) 67	R					x	3.59 μm	x		3	3.28 μm
C16H10 (pyrene) (85 K) 67	R					x	3.59 μm	x		3	3.28 μm
C6H5CO2H (benzoic acid) 107	R									0	3.20 μm
C6H5Cl (chlorobenzene) 108	T					x				1	3.25 μm
Asphaltite 21	R					x		x		2	3.38 μm
Kerite 21	R							x		1	3.42 μm
CH3NO (or HCONH2) (formamide) (10 K) 109	A					3.46 μm	3.57 μm			2	3.04 μm
HCOOH (formic acid) (ice deposited at 145 K, cooled down to 23 K) 110	A						3.59 μm	x		2	3.92 μm
C2H2O2 (glyoxal) (10 K) 91	A			2.91 μm		3.49 μm	3.59 μm	x		4	2.91, 3.49 μm (but also 3.26, 3.59, 3.74, 4.17, 4.26, 4.79 μm)
C2H2O2 (glyoxal) (80 K) 111	T			x		3.46&3.47 μm	3.57 μm			3	2.90, 3.46&3.47 μm (but also 3.26, 3.57, 3.60, 3.75, 3.92, 4.18, 4.46 & 4.67, 4.78 μm)
HOCH2–CHO (glycolaldehyde) (150 K) 89	A					x		x		2	3.09 μm
CH4N2O (urea or carbamide) 112	R	2.07 μm								1	2.22, 2.85 μm
C2H5NO2 (glycine) (85 K) 67	R	2.10 μm	2.54 μm	2.88 μm	3.01 μm	x				5	2.32, 2.45, 2.70, 3.40 μm (3.75 μm not visible for JIRAM)
C2H4O2 (acetic acid) (16 K) 113	A									0	3.30 μm
C2H4O o CH3CHO (acetaldehyde) (110 K) 114	A					x	3.57 μm			2	3.32, 3.50, 3.62, 3.64 μm
C40H80NO8P (L-alpha-phosphatidylcholine dipalmitoyl) (DPPC) 115	A									0	3.38, 3.43, 3.51 μm
EXOGENIC PRODUCTS											
O3 (ozone) (47 K) 116	A									0	3.29, 4.74, 4.88 μm
H2O2 (hydrogen peroxide) (80 K) 24	R									0	2.96, 3.34 μm, 3.15, 3.50 μm weaker
H2SO4 · H2O (hydrated sulfuric acid) (143 K, interval 2.5 – 5.0 μm) 117	A									0	3.44–3.92, 4.40 μm
H2SO4 · H2O (hydrated sulfuric acid) (80 K, interval 1.0 – 2.5 μm) 25	R									0	
H2CO (formaldehyde) (110 K) 95	A					3.47 μm	3.59 μm			2	3.00, 3.42, 4.27, 4.68 μm
H2CO3 (carbonic acid) (80 K) 94	A							x		1	3.09, 3.80 μm

List of chemical compounds investigated in this JIRAM data analysis, for which laboratory spectra in the 2–5 μm range exist in literature. Different horizontal sections respectively refer to volatile compounds, endogenic products (salt minerals and smectites), organic compounds, and exogenic products. Column A indicates the name of the compound and reference used to look for spectral signatures, plus the cryogenic temperature value if available (if no temperature value is reported, the compound is measured at room temperature). Column B indicates the measurement technique (R=reflectance, A=absorbance, T=transmittance). Columns C-J account for the spectral signatures observed by JIRAM: the green, yellow, and orange colours specify whether a given compound as measured in laboratory has a strong, medium, or weak absorption band at that wavelength, respectively. An 'x' symbol in a coloured cell means that the laboratory spectrum has a signature at the same wavelength as the signature measured by JIRAM. When a number is present, it indicates the exact wavelength of the minimum in the laboratory spectrum if it is within 20 nm of the signature measured by JIRAM. Blank cells mean that the compound has no spectral signatures at the wavelength measured by JIRAM, or that they deviate by more than 20 nm. Column K expresses the total number of positively identified signatures in the JIRAM data. Column L lists the strongest band in the spectral range between 2 and 5 μm: a light blue coloured box highlights that the strongest absorption matches one of the features detected by JIRAM.